Journal of Renewable and Sustainable Energy

# Servo-aero-gravo-elastic (SAGE) scaling and its application to a 13-MW downwind turbine

Cite as: J. Renewable Sustainable Energy **12**, 063301 (2020); https://doi.org/10.1063/5.0021171
Submitted: 08 July 2020 . Accepted: 08 October 2020 . Published Online: 04 November 2020

Meghan Kaminski, Eric Loth, Daniel Zalkind, Lucy Pao, Michael Selig, and Kathryn Johnson

Journal of Renewable and Sustainable Energy ARTICLE scitation.org/journal/rse

# Servo-aero-gravo-elastic (SAGE) scaling and its application to a 13-MW downwind turbine

Cite as: J. Renewable Sustainable Energy **12**, 063301 (2020); doi: 10.1063/5.0021171
Submitted: 8 July 2020 · Accepted: 8 October 2020 ·
Published Online: 4 November 2020

View Online Export Citation CrossMark

Meghan Kaminski,[1,a)] Eric Loth,[1] Daniel Zalkind,[2] Lucy Pao,[2] Michael Selig,[3] and Kathryn Johnson[4]

## AFFILIATIONS

[1]Department of Mechanical and Aerospace Engineering, University of Virginia, 122 Engineer's Way, Charlottesville, Virginia 22904, USA
[2]Department of Electrical Engineering, University of Colorado, 425 UCB, Boulder, Colorado 80309, USA
[3]University of Illinois at Urbana-Champagne, 104 S. Wright St., Urbana, Illinois 61801, USA
[4]Department of Electrical Engineering, Colorado School of Mines, 1500 Illinois Street, Golden, Colorado 80401, USA

[a)]Author to whom correspondence should be addressed: mek3xc@virginia.edu

## ABSTRACT

Reduced scale wind turbines can be extremely cost-effective to test new rotor concepts since prototype costs are heavily dependent on the rotor diameter. Ideally, the scaled model would have the same non-dimensional deflections, dynamics, and control behavior as the full-scale model. This would provide a high-fidelity demonstration of the full-scale performance, which is ideal if the full-scale turbine has significant aeroelastic interactions. To this end, servo-aero-gravo-elastic (SAGE) scaling is developed and applied to a 13-MW turbine that is scaled to a 20% scale model. The scaling preserves the tip-speed ratio, the rotor speed normalized by the flapping frequency, and the tip deflections normalized by the blade length. In addition, the controller employs the same control structure (gain-scheduled pitch control and variable speed torque control) and is scaled dynamically (e.g., matching non-dimensional time constant of the pitch angle, etc.). Furthermore, the thrust, gravity, and centrifugal moments are scaled such that the load angles are preserved as a function of a non-dimensional wind speed. However, the environmental scaling must consider differences in Reynolds number (since this parameter cannot be held constant) and subsequent changes in the axial induction factor. While the presented results showcase these differences during operational conditions, the non-dimensional tip deflections remain comparable through all wind speed ranges, indicating the viability of the SAGE scaling method in matching full-scale aeroelastic responses.



## NOMENCLATURE

| | |
|---|---|
| $a$ | Axial induction factor |
| $b$ | Speed of sound in air |
| $c$ | Chord length |
| $c_d$ | Airfoil coefficient of drag |
| $c_l$ | Airfoil coefficient of lift |
| $C_p$ | Turbine coefficient of power |
| $C_t$ | Turbine coefficient of thrust |
| $EI$ | Blade stiffness |
| $F$ | Blade forces |
| $Fr_{moment}$ | Moment-based Froude number |
| $g$ | Gravitational constant |
| $GK$ | Gain scheduling |
| $k_I$ | Integral gain |
| $k_P$ | Proportional gain |
| $Lo$ | Lock number |
| $m$ | Blade mass |
| $M$ | Moment |
| $Ma$ | Mach number |
| $N_{gear}$ | Gearbox ratio |
| $r$ | Distance |
| $Re$ | Reynolds number |
| $s$ | Spanwise location |
| $S$ | Total blade length |
| $U$ | Wind speed |
| $x$ | Airfoil chordwise distance |
| $y$ | Distance perpendicular to chord |
| $\alpha$ | Angle of attack |
| $\beta$ | Pre-cone angle |
| $\delta$ | Deflection |
| $\eta$ | Scaling factor |

| | |
|---|---|
| $\lambda$ | Tip-speed ratio |
| $\theta$ | Pitch |
| $\theta_k$ | Gain-scheduling parameter |
| $\rho$ | Density |
| $\tau$ | Shaft tilt |
| $\mu$ | Dynamic viscosity |
| $\psi$ | Azimuthal angle |
| $\dot{\varphi}$ | Rotor speed error |
| $\Omega$ | Angular speed of the rotor |
| $\omega$ | Blade Frequency |
| $\zeta$ | Regulator mode damping ratio |

## Subscripts

| | |
|---|---|
| $()_{1,2,3}$ | Coordinate frames |
| $()_c$ | Centrifugal |
| $()_{cmd}$ | Commanded |
| $()_{const}$ | Constant |
| $()_f$ | Full-scale value |
| $()_{flap}$ | Blade structural flapwise |
| $()_{fine}$ | Lower limit value |
| $()_{gear}$ | Gearbox value |
| $()_{gen}$ | Generator value |
| $()_{hub}$ | Hub value |
| $()_{infinity}$ | Free stream |
| $()_{local}$ | Local |
| $()_{max}$ | Maximum |
| $()_n$ | Regulator mode, natural |
| $()_{rated}$ | Rated value |
| $()_{rms}$ | Root-mean-square about mean |
| $()_{rot}$ | Rotating |
| $()_s$ | Sub-scale value |
| $()_{tower}$ | Tower |
| $()_{tip}$ | Tip value |
| $()_{wind}$ | Wind value |
| $()_\Omega$ | Value at specific rotational speed |
| $()'$ | Spanwise distributed value |
| $\overline{()}$ | Non-dimensional value |

## I. INTRODUCTION

Wind energy continues to grow and be a dominant force in the renewable energy sector with wind power having dramatic additions to the United States energy market.[1] Much of this growth is associated with an increase in turbine size (to capture the higher wind conditions at higher altitudes). The subsequent increase in blade length has led to increased flexibility and aeroelastic characteristics.[2] Examples of recent extreme-scale rotor designs [>10 MW (Refs. 3–6)] with such flexibility include the 13.2-MW SNL100 series[7–10] and the 13.2-MW segmented ultralight morphing rotor, denoted as the SUMR-13 turbine.[3,4,11–13] These designs employ blades more than 100 m in length providing dynamic responses, complex aerodynamics, and aeroelastics not typically seen in conventionally designed rotors. Since these designs have never been built, it is not clear to what degree current computational tools can adequately describe their behavior. Therefore, experimental results are critical for both testing and validation. To cost-effectively understand these dynamics under actual field conditions, scaled model prototypes can be designed, built, and tested prior to committing to the high cost of building the full-scale model.

A typical scaling method for the aeroelasticity and gravity effects on wind turbine blades is to use Froude scaling when going from the full-scale design to the sub-scale design.[14] However, such scaling does not take into account control characteristics nor the reduction in Reynolds number, resulting in models that do not permit the sub-scale model to replicate the aerodynamics of the full-scale model.[15,16]

In terms of controller scaling, it is well known that the controller architecture and parameters can substantially change the root bending moments and thus blade dynamics and deflections.[17] However, to the authors' knowledge, there are no previous studies addressing controller scaling performance for extreme-scale wind turbines using a full aeroelastic deflection case.

In terms of the Reynolds number issue, McTavis *et al.*[18] investigated the wake and coefficient of thrust effects on turbines for a Reynolds number range of $10^4$–$10^5$. They experimentally compared a turbine with a 1.2 m diameter rotor (operating at a Reynolds number of 175 000) with a smaller sub-scale turbine with a 25 cm diameter rotor operating at Reynolds numbers of 29 100 and 12 800. The results showed that the smallest Reynolds number sub-scale model has a coefficient of thrust that is 60% less than that of the full-scale rotor, while the moderate Reynolds number sub-scale model has a 25% deficit. Similarly, Make and Vaz[19] used simulations to investigate various sub-scale rotors with matching tip-speed ratios. The first sub-scale model was geometrically scaled while the second model was scaled to match the full-scale performance by altering the chord length, twist distribution, and distributed airfoils. The geometrically scaled turbine yielded a 50% thrust deficit with five times less power due to the differences in Reynolds number and its effect on the blade lift and drag. However, these differences are lessened when employing the performance-based model. These studies show that the effects of Reynolds number when applying aeroelastic sub-scaling to a wind turbine can be important.

Another such test which applies a gravo-aeroelastic scaling approach is a 20% demonstrator of the 13.2-MW segmented ultralight morphing rotor (SUMR-13) suitable for testing at the National Wind Technology Center (NWTC).[20,21] The test presents differences in manufacturing and site-specific constraints such that while the full-scale turbine is optimized for class IIB wind speeds, the scale model is designed to withstand class IA wind speeds, which contain both higher scaled wind speeds and turbulence intensity. These conditions cause the scale model to be designed with above ideal mass and stiffness distributions that therefore affect the aerostructural interactions.

The following investigation documented in this article develops a physically scaled computational 20% model of the SUMR-13 system by placing it in an ideal environment (wind speeds and turbulence intensity) and matching the following full-scale non-dimensionalized parameters: tip-speed ratio, tip deflection relative to blade length, and rotor frequency relative to the flapping frequency. Furthermore, a total rotational Froude number and sectional rotational Loch number are defined and held constant between sub- and full-scale systems. In addition, the non-dimensional controller performance is ideally replicated in the sub-scale system. The sub-scale demonstrator used for this study is termed herein as segmented ultralight morphing rotor-physically scaled (SUMR-PS). A consequence of the gravo-aeroelastic scaling is the mismatch of Reynolds numbers between full- and sub-

scales, resulting in differences in aerodynamic performance whose effects on operation will be explored.

Thus, the goal of this study is to develop a scaling approach that can have the same non-dimensional deflections, dynamics, and control behavior to provide a high-fidelity demonstration of a full-scale turbine with significant aeroelastic behaviors. To this end, a servo-aero-gravo-elastic (SAGE) scaling approach is developed and applied to a 13-MW turbine scaled down to 20% of the full-scale dimensions. All the critical servo-gravo-aeroelastic non-dimensional parameters are held constant during this scaling. For such scaling, the Reynolds number cannot be held constant and the magnitude of the Reynolds number effect is investigated by running the SUMR-PS turbine with airfoil coefficients of the SUMR-13 rotor. This model will be denoted the SUMR-aerodynamically scaled (SUMR-AS) model.

While force-based Froude scaling has been previously employed in many engineering systems, this is the first (to the authors' knowledge) Froude scaling developed and employed for the rotor moments for an extreme-scale turbine. It is also the first investigation of Froude scaling developed and employed for the rotor moments for an extreme-scale turbine. It is also the first investigation of Froude scaling combined with aeroelastic scaling or with control-based scaling for a wind turbine rotor blade and the first to do such simulations under operational turbulent field conditions. It is also the first study to employ a servo-aero-gravo-elastic scaling method to an extreme-scale wind turbine and the first to examine the effects of the Reynolds number mismatch. Furthermore, this is the first study which explores a computationally scaled rotor which applies to each of the structural components, aerodynamics, and control systems on the wind turbine. The comparison between a full-scale model and a sub-scale model is herein accomplished computationally as an experimental comparison with a full-scale 13.2-MW turbine would be extremely expensive (as will be discussed), but the results can be used to develop an experimentally scaled campaign and understand the expected effects due to Reynolds number.

This article is organized as follows. Section II explains the generalized SAGE method. Section III applies the SAGE method to the SUMR-13 turbine to define scaled geometry with influence on sectional aerodynamics as well as to scale blade mass, blade stiffness, incoming wind speeds, and controller parameters. Section IV evaluates the performance of the scaling in terms of operational rotor performance and blade deflections. Finally, Sec. V provides concluding remarks and recommendations for future studies.

## II. GENERAL SERVO-AERO-GRAVO-ELASTIC SCALING METHODS

To create a servo-aero-gravo-elastic model, one must appropriately scale the structural, wind, and controller parameters individually. A geometric scaling factor ($\eta$) is first defined as the ratio of the full-scale blade length ($S_f$) to the sub-scale blade length ($S_s$),

$$\eta = \frac{S_s}{S_f}. \tag{1}$$

The aforementioned scaling factor is applied to all geometric external dimensions: hub radius ($r_{hub}$), spanwise location along the blade length ($s$), chord (c), etc. To further ensure geometric similitude, any angle associated with the wind turbine must remain constant such as: coning angle ($\beta$), shaft tilt ($\tau$), azimuthal angle ($\psi$), etc., as shown

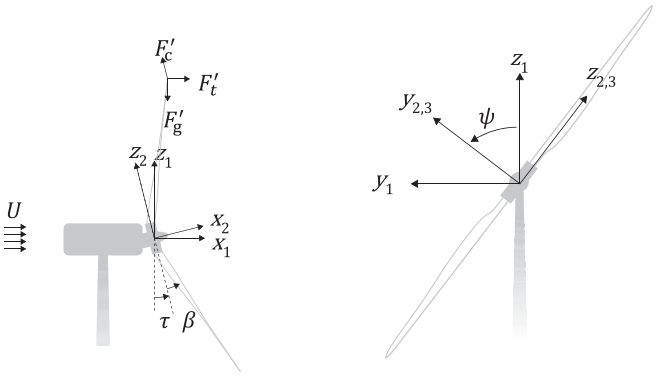


(a) Side View (b) Facing Downwind

**FIG. 1.** Turbine depicted from (a) the side view and (b) the front view facing downwind with parameters and sectional moments shown: blade pre-cone angle ($\beta$), shaft tilt ($\tau$), azimuth position ($\psi$), incoming wind speed ($U$), sectional centrifugal force ($F_c'$), sectional thrust force ($F_t'$), and sectional gravitational force ($F_g'$).

in Fig. 1 with three reference coordinate frames denoted with the subscripts 1, 2, and 3. Coordinate frame 1 is fixed to the nacelle of the turbine in which the gravitational force is aligned in the negative $z_1$-direction. Coordinate frame 2 is a rotating coordinate system attached to the hub of the rotor in which the blade centrifugal force is aligned with the $z_2$-direction. Coordinate frame 3 is attached to the root of the blade which differs from frame 2 through a blade coning angle. A summarization of the three coordinate frames pictured can be found in Kaminski *et al.*[22]

Next, we consider the contributions to the root flapwise bending moment ($M$), which are dependent on the sectional distributed forces ($F$). Retaining the ratio of the centrifugal component ($M_c$) to the gravitational component ($M_g$) between full- and sub-scale allows for matching structural load angles along the blade. The ratio of centrifugal to gravitational moments is expressed herein based on the acceleration due to gravity ($g$) acting on the blade pointed upwards ($\psi = 0$) as shown in Fig. 1,

$$\frac{M_c}{M_g} = \frac{\Omega^2 (r_{hub} + S\cos\beta)\sin\beta}{g\,(\cos\beta\sin\tau - \sin\beta\cos\tau)}. \tag{2}$$

The right-hand-side of this equation is derived in terms of coning and shaft tilt angles and integrated along the span. Holding this moment ratio fixed ensures that the load angles associated with the combination of the gravity and centrifugal effects on the blades will be preserved as a function of the azimuth angular position $\psi$. While Eq. (2) has been defined for $\psi = 0$, similar arguments can be used for other azimuthal locations and lead to the same scaling ratios. If the shaft tilt and coning angle are preserved, then keeping the moment ratio fixed requires that $\Omega^2 S/g$ is preserved, which can be defined as a rotational Froude number ($Fr_{rot}$) as

$$Fr_{rot} = \frac{\Omega^2 S}{g} = \frac{M_c}{M_g}. \tag{3}$$

If the geometric angles as well as the ratio of hub radius to blade radius are preserved, it can be seen that preserving this rotational Froude number of Eq. (3) is equivalent to preserving the moment ratio of

Eq. (2). Note that this differs from a Froude number (ratio of inertial and gravitational forces) due to the rotational Froude number being a ratio of centrifugal and gravitational moments. The relationship between centrifugal and gravitational moments dictates the rotational speed scaling which is shown as follows:

$$\frac{\Omega_s}{\Omega_f} = \frac{1}{\sqrt{\eta}}. \tag{4}$$

Fixing the tip-speed ratio preserves the flow angles and dynamics. Applying appropriate length and rotational speed scaling to the fixed tip-speed ratio, the upstream wind speed ($U$) scaling can be found. The following defines the tip-speed ratio ($\lambda$) and the wind speed scaling:

$$\lambda = \frac{\Omega(r_{hub} + S\cos\beta)}{U}, \tag{5}$$

$$\frac{U_s}{U_f} = \sqrt{\eta}. \tag{6}$$

Given that time scales ($t$) will be proportional to the ratio of the length to the velocity scales, this indicates that the dynamics in the sub-scale time variation must be scaled as seen as follows:

$$\frac{t_s}{t_f} = \sqrt{\eta}. \tag{7}$$

Next, one should consider the influence of the thrust component, by taking the ratio of the sectional centrifugal component ($M_c'$) of the flapwise bending moment relative to the thrust component ($M_t'$) of the flapwise bending moment. The centrifugal component occurs in the opposite of the thrust component when the azimuthal angle is zero ($\Psi = 0$) and is a function of the rotor speed, distance from the center of rotation, and the blade coning angle. The thrust component in the denominator is a function of the sectional thrust component ($c_t$), the sectional chord length ($c$), and the relative wind velocity as a combination of the incoming windspeed and the turbine rotational speed. Additionally, the turbine thrust is defined to be aligned with the nacelle-fixed coordinate system. To align the thrust component with a rotating blade fixed system which aligns with the centrifugal component, the thrust force is rotated through the shaft tilt, blade azimuth position, and the blade coning angle. Further explanation of the transformation can be found in Kaminski *et al.*,[22]

$$\frac{M_c'}{M_t'} = \frac{-m'\Omega^2(r_{hub} + s\cos\beta)\sin\beta}{\frac{1}{2}\rho_{wind}C_t c\left(U_{rated}^2 + [\Omega\{r_{hub} + s\cos(\beta - \tau)\}]^2\right) * (\cos\tau\cos\beta - \sin\tau\cos\psi\sin\beta)}. \tag{8}$$

Equation (8) is simplified by retaining the structural angles, applying the geometric scaling of Eq. (1), and keeping the tip-speed ratio constant between full- and sub-scale systems. Based on the above result, one may define a sectional rotational Lock number as

$$Lo_{rot}{}' = \frac{m'\Omega^2}{\rho_{wind}c_t U_{rated}^2}. \tag{9}$$

Note that this differs from a Lock number (ratio of aerodynamic and inertial loads of a full blade) as it is a ratio of centrifugal and aerodynamic loads for a section of the blade. If the geometric angles as well as the ratio of hub radius to blade radius are preserved, it can be seen that preserving this rotational Lock number of Eq. (9) at each spanwise station is equivalent to preserving the sectional moment ratio of Eq. (8). Note that Eq. (9) is proportional to the square of the tip-speed ratio but varies as a function of non-dimensional span.

Retaining Eq. (9) and applying an assumption of constant coefficient of thrust between full- and sub-scale systems, the sectional blade mass density is found to scale with the ratio of the air densities and $\eta^2$. Integrating these sectional values along the span of the blade leads to the total blade mass scaling. The sectional and total blade mass scale as follows:

$$\frac{m_s'}{m_f'} = \left(\frac{\rho_{wind,s}}{\rho_{wind,f}}\right)\eta^2, \tag{10}$$

$$\frac{m_s}{m_f} = \left(\frac{\rho_{wind,s}}{\rho_{wind,f}}\right)\eta^3. \tag{11}$$

The significance of the presence of the changes in density of the wind is a direct response to Eq. (9) and its attempts to match a ratio of a mass specific quantity and an aerodynamic quantity. Therefore, if the sub-scale system is operating in an environment with a lower air density, it should follow that the mass of the system should also have a lower than ideal sub-scale mass.

Based on the above, the scaling for the key base units is summarized in Table I and the application to several key parameter ratios is listed in Table II, based on the above analysis and assuming all variables can scale perfectly, as would be ideal. The Reynolds and Mach numbers at a given spanwise location are conventionally defined based on the local chord and local freestream velocity. However, this is generally not possible for Reynolds and Mach numbers as field testing does not allow adjustment of the viscosity nor the speed of sound of the surrounding air. This can cause a difference in both the Reynolds number and the Mach number, which effects the turbine aerodynamic performance. It is hypothesized that these effects are weak, even for

**TABLE I.** Base unit scaling in terms of the length scaling parameters, $\eta$.

| Base units, SI units | Scale factor |
|---|---|
| Length | $\eta$ |
| Time | $\sqrt{\eta}$ |
| Mass | $\left(\frac{\rho_{wind,s}}{\rho_{wind,f}}\right)\eta^3$ |

**TABLE II.** Summary of key structural and aerodynamic scaling parameters in terms of the length scaling parameter, $\eta$.

| Scaling parameter | Scale factor |
|---|---|
| Length scaling: $S_s/S_f$ | $\eta$ |
| Rotational scaling: $\Omega_s/\Omega_f$ | $1/\sqrt{\eta}$ |
| Wind velocity scaling: $U_s/U_f$ | $\sqrt{\eta}$ |
| Sectional blade mass scaling: $m_s/m_f$ | $\left(\frac{\rho_{wind,s}}{\rho_{wind,f}}\right)\eta^2$ |
| Flapwise frequency scaling: $\omega_{flap,s}/\omega_{flap,f}$ | $1/\sqrt{\eta}$ |
| Stiffness scaling: $(EI')_s/(EI')_f$ | $\left(\frac{\rho_{wind,s}}{\rho_{wind,f}}\right)\eta^5$ |
| Bending moment scaling: $(M)_s/(M)_f$ | $\left(\frac{\rho_{wind,s}}{\rho_{wind,f}}\right)\eta^4$ |
| Power scaling: $(P)_s/(P)_f$ | $\left(\frac{\rho_{wind,s}}{\rho_{wind,f}}\right)\eta^{7/2}$ |
| Reynolds number ratio: $Re_s/Re_f$ | $\left(\frac{\rho_{wind,s}}{\rho_{wind,f}}\right)\left(\frac{\mu_{wind,f}}{\mu_{wind,s}}\right)\eta^{3/2}$ |
| Mach number ratio: $Ma_s/Ma_f$ | $\left(\frac{b_{wind,f}}{b_{wind,s}}\right)\sqrt{\eta}$ |

advanced-design extreme-scale wind turbines. The present study seeks to evaluate that hypothesis.

Beyond the structural and aerodynamic parameters, the controller must also scale appropriately. The structure of the control system is consistent from full- to sub-scales, i.e., the full-scale and scale systems both contain a gain-scheduled proportional–integral (PI) pitch control and a variable-speed torque controller similar to that of the NREL-5MW reference controller.[23] As mentioned, it is important to maintain the tip-speed ratio ($\lambda$) defined in Eq. (5) and the non-dimensional rotational rate frequency ($\overline{\Omega_{flap}}$) in order to retain consistent flow angles over the blade as well as maintain the input to output frequencies of the rotor (blade natural frequency to the rotational frequency)

$$\overline{\Omega_{flap}} = \frac{\Omega}{\omega_{flap,\Omega}}. \tag{12}$$

The pitch control dynamics directly affect flapwise loading,[24–27] so the pitch response of the rotor (to an incoming wind gust) must be consistent between the full- and sub-scale rotor models. The pitch angle ($\theta$) control is a commonly used gain-scheduled, proportional–integral control law,[23,28] defined by

$$\theta_{cmd,\Omega} = GK(\theta)\left[k_P N_{gear}(\Omega - \Omega_{rated}) + k_I N_{gear}\int(\Omega - \Omega_{rated})dt\right], \tag{13}$$

where $k_P$ and $k_I$ are the proportional and integral gains (which are functions of both the pitch control natural frequency, $\omega_n$, and the damping ratio, $\zeta$), $\Omega$ is the rotor speed, $N_{gear}$ is the gearbox ratio, and $\Omega_{rated}$ is the rated speed. The gain-scheduling term

$$GK(\theta) = \frac{1}{1 + \frac{\theta}{\theta_k}}, \tag{14}$$

accounts for aerodynamic non-linearities and depends on the blade pitch $\theta$ and the gain scheduling parameter $\theta_k$. The blade pitch command in Eq. (13) is saturated at a lower limit of $\theta_{fine}$, the aerodynamically optimal pitch angle. When a rigid body rotor model is combined with the PI control in (13), the dynamics of the generator speed error can be represented by a second order system[23]

$$\ddot{\varphi}_\Omega + 2\zeta\omega_n\dot{\varphi}_\Omega + \omega_n^2\varphi_\Omega = 0, \tag{15}$$

which is similar to the dynamics of the pitch response because $\dot{\varphi}_\Omega = \Omega - \Omega_{rated}$ and the pitch command in Eq. (13) is a linear combination of $\varphi_\Omega$ and its derivatives.

The pitch response is made consistent by matching the non-dimensional time constant of the pitch angle or the time it takes the pitch to transition 63% of the difference between the initial and final values during a step increase in wind speed. The time constants are a result of scaling the regulator mode natural frequency ($\omega_n$) as defined in Table III. Using the base unit scaling of Table I, the expected time constants should scale with $\sqrt{\eta}$. By matching the time constants due to a deterministic step increase in wind speed, it is expected that the dynamics of the sub-scale system will match the full-scale system during turbulent conditions as well.

The turbine is tested using FAST, an aeroelastic simulation tool that uses blade element momentum theory.[19,29] The two-dimensional aerodynamic parameter files will be presented herein, which show the coefficient of lift ($c_l$) and coefficient of drag ($c_d$) vs the airfoil angle of attack (AOA) ($\alpha$) at 66% span for the full-scale and sub-scale Reynolds numbers. The 66% span location is used for the aerodynamic properties as this is near where the effective radius for the thrust root bending moment is typically located.

The appropriate structural, wind speed, controller, and two-dimensional aerodynamic parameter files will be used to return the three-dimensional results via simulation. These results will display the differences due to Reynolds number under both steady and turbulent conditions.

## III. SCALING APPLIED TO AN EXTREME-SCALE TURBINE

### A. Scaling summary

The overall scaling is summarized in Table IV, where the turbine utilized for the full-scale model is the SUMR-13 rotor with 104.36 m blades and a tower height of 142.4 m. When a scaling factor of 0.2 ($\eta = 0.2$) is applied to the full-scale model, the sub-scale rotor has blade lengths of 20.87 m and a tower height of 28.48 m. This scaling leads to a sub-scale blade mass which is 1/150th the mass of the full-scale blade. This physically scale sub-scale model is deemed the

**TABLE III.** Dimensional controller scaling parameters for a servo-aero-gravo-elastic model.

| Scaling parameter | Scale factor |
|---|---|
| Time constant, $t_{const}$ | $\sqrt{\eta}$ |
| Pitch control natural frequency, $\omega_n$ | $1/\sqrt{\eta}$ |
| Gain scheduling parameter, $\theta_k$ | 1 |
| Damping ratio, $\zeta$ | 1 |

**TABLE IV.** Summarizing parameters of the SUMR-13 rotor, the servo-aero-gravo-elastically scaled SUMR-PS turbine, and the aerodynamically scale SUMR-PS turbine.

| | SUMR-13 | SUMR-PS | SUMR-AS |
|---|---|---|---|
| Length scaling factor ($\eta$) | 1 | 0.2 | 0.2 |
| Blade length ($S$) | 104.36 m | 20.87 m | 20.87 m |
| Hub radius ($l_{hub}$) | 2.5 m | 0.5 m | 0.5 m |
| Tower height ($l_{tower}$) | 142.4 m | 28.48 m | 28.48 m |
| Coning angle ($\beta$) | Variable | 12.5° | 12.5° |
| Tip-speed ratio ($\lambda$) | 9.5 | 9.5 | 9.5 |
| Rated turbine power ($P_{rated}$) | 13.2 MW | 47 kW | 47 kW |
| Rated wind speed ($U_{rated}$) | 11.3 m/s | 5.05 m/s | 5.05 m/s |
| Rated rotor speed ($\Omega_{rated}$) | 9.82 rpm | 21.96 rpm | 21.96 rpm |
| Pitch saturation ($\theta$) | 0.48° | 0.48° | 0.48° |
| Blade mass ($m$) | 54 787.4 kg | 350.64 kg | 350.64 kg |
| Flapping frequency ($\omega_{flap}$) at $\Omega_{rat}$ | 0.69 Hz | 1.53 Hz | 1.53 Hz |
| Reynolds number at 66% span ($Re$) | $1.63 \times 10^7$ | $1.16 \times 10^6$ | $1.63 \times 10^7$ |
| Ref. Mach number at 66% span ($Ma$) | 0.227 | 0.101 | 0.227 |

segmented ultralight morphing rotor-physically scaled and includes a physically scaled blade model and a physically scaled environment.

A caveat to testing a scaled model within a scaled environment is the presented differences in both the Reynolds numbers and Mach numbers. The Mach numbers are expected to have minimal effect on turbine performance, given that the turbine Mach numbers are below that of when compressibility comes into effect and therefore the resulting differences are weak. However, while testing in the same medium, the Reynolds numbers will be mismatched, which ultimately results in differing aerodynamic performances between full- and sub-scale systems. To ensure that the operational differences in the SUMR-PS model are reliant on differences in Reynolds number, an aerodynamically scaled turbine will also be compared against the full-scale model. This aerodynamically scaled model utilizes the SUMR-PS blade model; however, it employs airfoil coefficients of the full-scale model so as to eliminate the differences in Reynolds numbers. Each of the blade model and aerodynamic characters of the SUMR-13, SUMR-PS, and SUMR-IS turbines are summarized in Table IV.

## B. Rotor airfoil shapes and sectional aerodynamics

The full-scale rotor used for the current SAGE model is the 13.2-MW segmented ultralight morphing rotor (SUMR-13).[3,4,11–13] The SUMR-13 rotor is a two-bladed downwind morphing rotor with blade lengths reaching to 104.4 m. Select airfoils distributed down the length of the blades are shown in Fig. 2. Adjacent airfoils are used to define additional airfoils at intermediate locations. The SUMR-13 turbine represents a class of turbine blades denoted as extreme-scale wind turbine blades which, along with having excessive length, are highly flexible causing additional dynamics not represented in conventional wind turbine blades. The SUMR-PS and SUMR-AS turbines employ similar geometric properties as the SUMR-13 turbine including the airfoil distribution shown in Fig. 2, the non-dimensional chord distribution, and the twist distribution. However, the SUMR-PS has an aerodynamic performance based on the reduced Reynolds numbers where the SUMR-AS has an aerodynamic performance based on the full-scale Reynolds number. Each of the physical aerodynamic properties of the full-scale SUMR-13 system are summarized in Ananda *et al.*[4]

While the SUMR-PS employs geometric similitude (as shown) as well as properly scale frequencies, controllers, stiffness, and mass distribution (as discussed below), the aerodynamic performance will not scale properly. In particular, differences in Reynolds numbers will cause the airfoil lift and drag (as a function of angle of attack) to be modified. These difference are used by FAST and are based on data synthesized between experiments and XFOIL.[30] Shown in Fig. 3 are the coefficients of lift and drag as a function of angle of attack for an airfoil at 66% span. The airfoil utilized is a blend between the 56% and 77% span airfoils found in Fig. 2. The SUMR-13 rotor operates at a higher Reynolds number than that of the SUMR-PS turbine causing a decrease in lift as well as an increase in drag which holds true for all airfoils along the blade span. Therefore, in operation, the entire blade will experience a decrease in lift and an increase in drag if the two blades are operating at the same angle of attack (AOA).

## C. Blade mass and stiffness distributions

Based on Table II, the flapwise sectional properties of stiffness ($EI'$) and mass density ($m'$) are non-dimensionally matched in Eqs. (16)–(18) where the overbar ($\bar{}$) represents non-dimensional values. Their values are presented in Fig. 4 as a function of the non-dimensional spanwise location

$$\bar{s} = \frac{s}{S}, \tag{16}$$

$$\overline{EI'} = \frac{EI'}{\rho_{wind} g S^5}, \tag{17}$$

$$\overline{m'} = \frac{m'}{\rho_{wind} S^2}. \tag{18}$$

## D. Empirically scaled controller and scaled wind flowfield

To verify the controller scaling, a non-dimensional step input of wind speeds is applied to each turbine in order to check the non-dimensional time constant of the pitch angle in response to a step

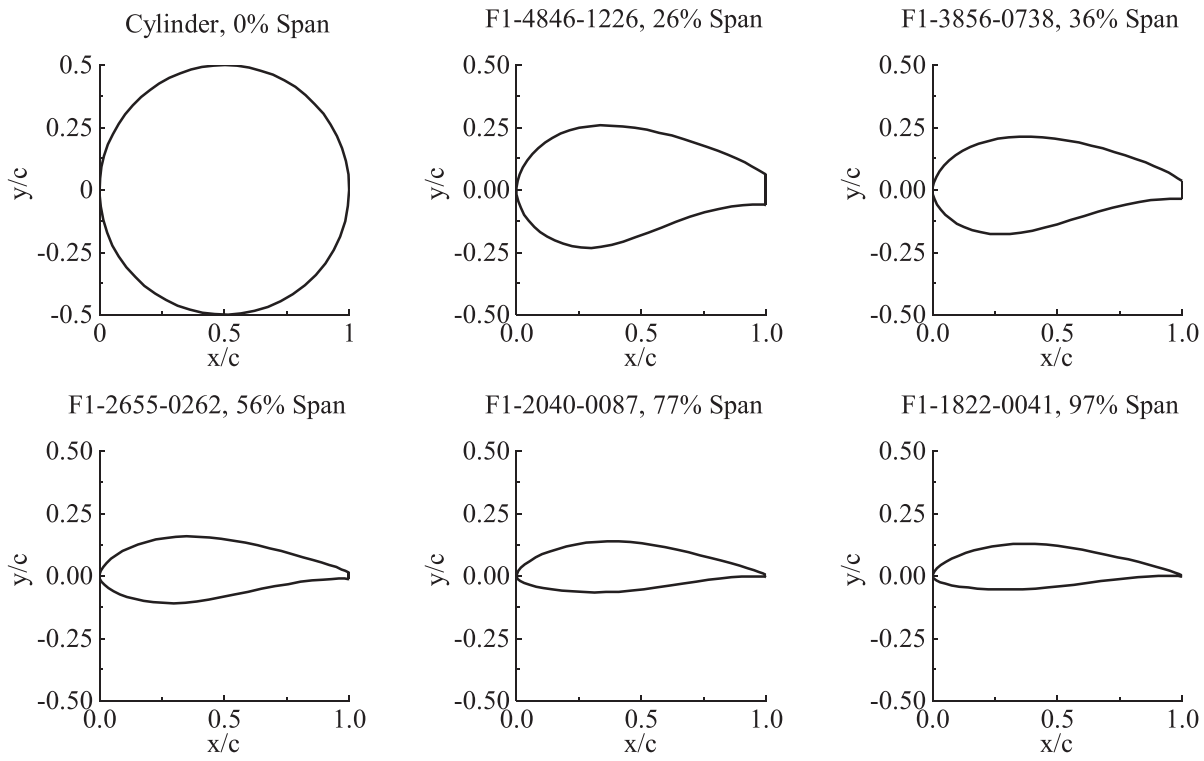


**FIG. 2.** Airfoil distribution of the SUMR-13, SUMR-PS, and SUMR-AS rotors shown non-dimensionally by the chord length *c*, the distance along the chord *x*, and the distance perpendicular to the chord *y*. Each blade employs the same non-dimensional chord and twist distributions.

change in wind speed. A non-dimensional wind input step size of 0.265 will be applied to starting non-dimensional wind speeds of 1.327 and 1.77, i.e., 33% and 77% above rated. The non-dimensional wind speed values utilize Eq. (19) and are plotted against non-dimensional time of equation (20) shown in Fig. 5. These values are chosen in order to provide a full-range of above-rated operating conditions

$$\overline{U} = \frac{U}{U_{\text{rated}}}, \tag{19}$$

$$\overline{t} = t * \frac{g}{U_{\text{rated}}}. \tag{20}$$

The controller variables are then scaled as stated in Table III with the resulting parameters summarized in Table V. Table V additionally

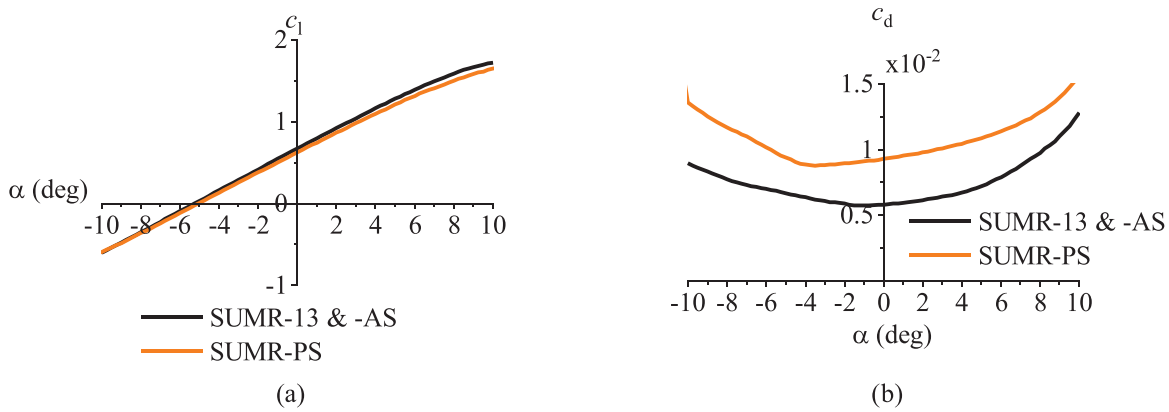


**FIG. 3.** The (a) coefficients of lift ($c_l$) and (b) coefficients of drag ($c_d$) vs airfoil angle of attack ($\alpha$) for the full-scale SUMR-13 turbine, the physically scaled SUMR-PS turbine, and the aerodynamically scaled SUMR-AS turbine for an airfoil at 66% span with Reynolds numbers shown in Table IV, where the airfoil properties are linearly interpolated between the F1-2655-0262 and the F1-2040-0087 airfoils.

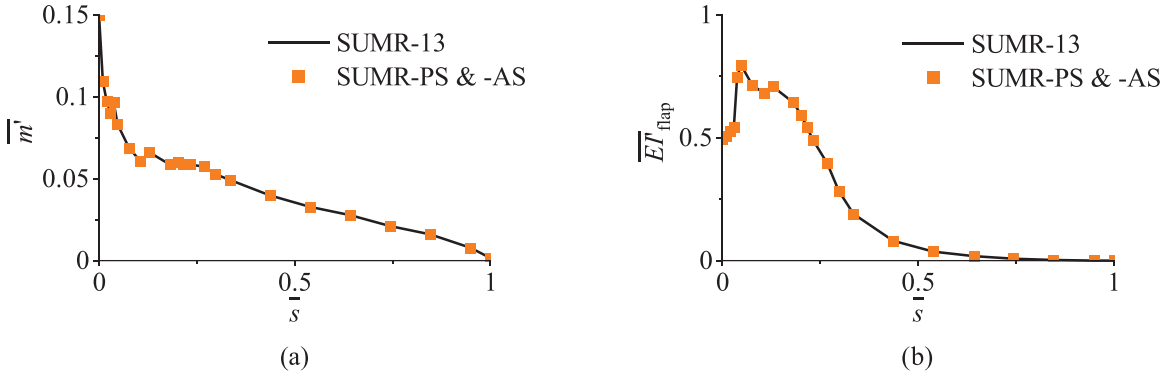


**FIG. 4.** Select non-dimensional distributed blade structural parameters for (a) mass density ($\bar{m}'$) and (b) stiffness ($\bar{EI}'$) for the SUMR-13 blade, the physically scaled SUMR-PS blade, and the aerodynamically scaled SUMR-AS blade.

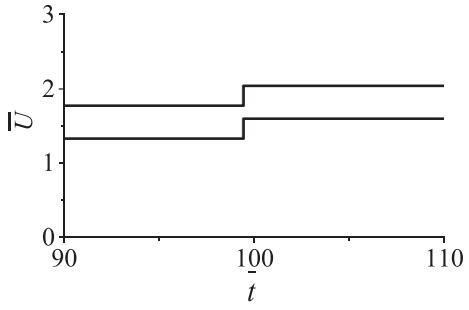


**FIG. 5.** Two non-dimensional input wind speeds spanning the region 3 operating regime for verifying the controller scaling performance.

contains the non-dimensional time constant of the pitch angle (time for pitch to reach 63% of its final pitch) for the SUMR-13, the SUMR-PS, and the SUMR-AS controllers. The pitch angle as a result of the step changes in wind speed can also be seen in Fig. 6 where there is a ∼5.5% error in the non-dimensional time constant. The error in time constant can be attributed to the assumption of a rigid body rotor model used for Eq. (15). The results shown in Fig. 6 indicate that there can be small controller differences which can be related to the effects of aeroelasticity and Reynolds numbers. A future recommendation is to provide additional adjustments to reduce, or even eliminate, these pitch response differences and more generally the rotor speed dynamics relative to natural frequency and damping. However, an important conclusion is that the servo-response can be reasonably scaled using the non-iterative method described herein. In general, the controller for the SUMR-PS and SUMR-AS models in terms of pitch response to this discontinuous velocity shift is about 5%–10% less responsive that that of the SUMR-13 in terms of non-dimensional time response.

For a final scaling check, we consider the wind speeds. Since the turbines are tested under turbulent conditions, it is important to ensure that the scaled mean and fluctuation inflow parameters are preserved as well as match the coherence method of the full- and sub-scale inputs. If one considers a fixed wind site with given atmospheric boundary layer properties (including characteristic variations in shear with altitude), there will be some differences in the unsteady inflow velocity field seen by the sub-scale and full-scale turbines due to changes in the hub-height relative to this flow. However, one may sample data which have the same non-dimensional mean and RMS hub-height velocities to evaluate the fidelity of field-test operational scaling.

Using a mean velocity profile for the Virginia Offshore Lease Zone (for which the SUMR-13 was designed), the scaled hub-height wind velocities for the sub-scale and full-scale rotor are shown as a

**TABLE V.** Summarizing parameters of the SUMR-13, SUMR-PS, and SUMR-AS (with adjusted controllers) with their respective non-dimensional time constants due to a non-dimensional step steady-state wind speed input.

| | | | Non-dimensional | Windspeed range |
|---|---|---|---|---|
| | $\Omega_n$ (rad/s) | $\xi$ (–) | 1.38–1.59 $\bar{t}_{\text{const}}$ | 1.77–2.04 |
| SUMR-13 | 0.1415 | 1.35 | 5.31 | 7.10 |
| SUMR-PS | 0.316 | 1.35 | 5.60 | 7.47 |
| SUMR-AS | 0.316 | 1.35 | 5.60 | 7.47 |

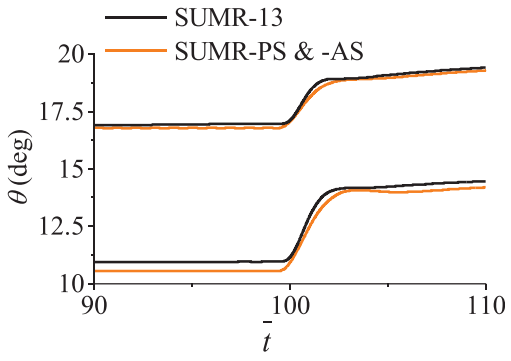


**FIG. 6.** Comparison of the physically scaled controller pitch ($\theta$) over a non-dimensional time subjected to two separate step input wind speeds as specified in Fig. 5 which span the region 3 operating regime.

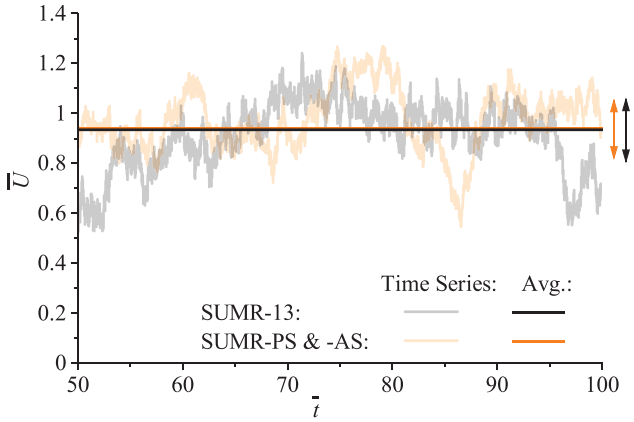


**FIG. 7.** Example non-dimensional wind input ($\bar{U}$) with simulation average velocities (solid lines) and the range of ± one standard deviation (vertical arrow) shown as a function of non-dimensional time ($\bar{t}$) for computational simulations.

function of the non-dimensional time in Fig. 7. In both cases, TurbSim[31] is employed to provide a full three-dimensional coherent unsteady wind field inputs for FAST.[29] While instantaneous values are different, the mean and standard deviations are nearly identical and thus deemed suitable for direct comparison. However, it should be noted that choosing a specific site for both the sub-scale and the full-scale rotors will lead to differences in the local shear and turbulence scales once these are normalized by hub-height or rotor diameter. It is hypothesized that these effects, along with those seen in Fig. 6, are weak with respect to the non-dimensional flapwise deflections and dynamics of the rotor blades.

## IV. OPERATIONAL RESULTS OF A SCALED TURBINE

### A. Rotor aerodynamic performance

The reduction in Reynolds number on the appropriately scaled two-dimensional airfoils leads to a slight decrease in lift and a large increase in drag for the same operating angle of attack as shown in Fig. 3. As summarized in Sec. III, the turbine saturates the blade pitch at its lower limit under below-rated conditions to maximize power capture and regulates power production under above-rated conditions by regulating the rotor speed. The relationship between the turbine coefficient of power and the coefficients of lift and drag are shown in Eq. (21) and the subsequent relationship between the coefficient of power and axial induction factor are shown in Eq. (22),[32]

$$C_p = C_l\sqrt{1+\lambda^2}\left(\lambda - \frac{C_d}{C_l}\lambda^2\right), \tag{21}$$

$$C_p = 4a(1-a)^2. \tag{22}$$

The relationship shown in Eq. (21) includes the turbine tip-speed ratio $\lambda$. The tip-speed ratio is maintained through scaling shown in Fig. 8(a) despite the slight reduction in coefficient of lift and a significant increase in coefficient of drag due to Reynolds numbers differences. These differences cause the axial induction factor to substantially decrease for the outboard regions as seen in Fig. 8(b) for region 2 operations with steady flow. To understand the effects of the Reynolds number on the operational outcome of the SUMR-PS model, the results are compared against the SUMR-AS model. As a reminder, the SUMR-AS model utilizes the same turbine as the SUMR-PS model; however, it employs the same aerodynamics coefficients as the SUMR-13 rotor, thus eliminating any differences in the Reynolds number.

The SUMR-13 rotor is designed to operate at the maximum coefficient of power as seen in Fig. 9. For the SUMR-PS model, there is a reduction in maximum coefficient of power and thrust in region 2 on the rotor as expected through Figs. 3 and 8. To investigate the influence of the Reynolds number on the results, the SUMR-AS model is compared against the SUMR-13 and SUMR-PS models with minimal differences between the SUMR-13 and SUMR-AS models. These results helps to justify the differences between the SUMR-13 and SUMR-PS models being solely due to the Reynolds number differences within the scale model.

A summary of the influence of the Reynolds number difference is depicted in Fig. 10 and seen under below-rated conditions. When scaling down the turbine, the Reynolds number decreases, which leads to a decrease in the lift and an increase in the drag of the blade airfoils. These two-dimensional aerodynamic effects then result in a reduction in the axial induction factor due to the reduction in torque, thus reducing the turbine coefficient of power. These aerodynamic changes lead to operational changes in the turbines as will be discussed in Sec. IV B.

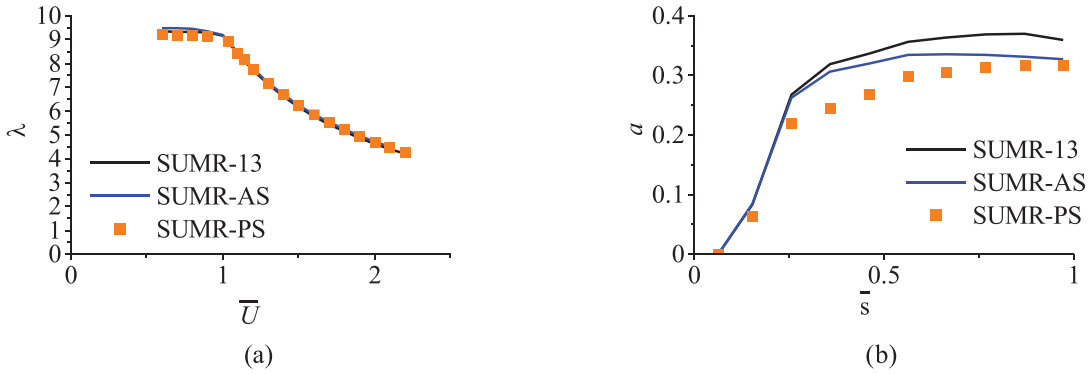


**FIG. 8.** Computational results with steady flow of (a) the tip-speed ratio over a range of operating conditions and (b) the turbine axial induction factor under below rated conditions where $\bar{U} = 0.7$ over the span of the blade.

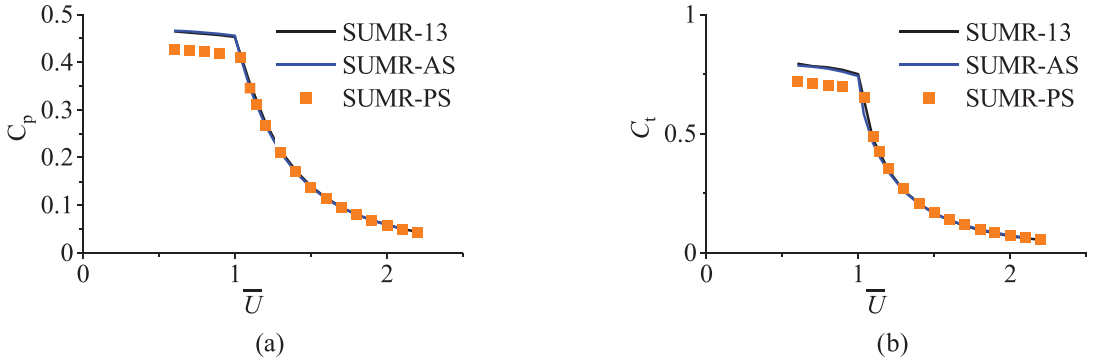


**FIG. 9.** The (a) turbine coefficient of power ($C_p$) and (b) turbine coefficient of thrust ($C_p$) in steady flow over the entire range of operating conditions comparing the SUMR-13, the SUMR-PS, and the SUMR-AS, a physically scaled model simulating with removal of Reynolds number coefficients.

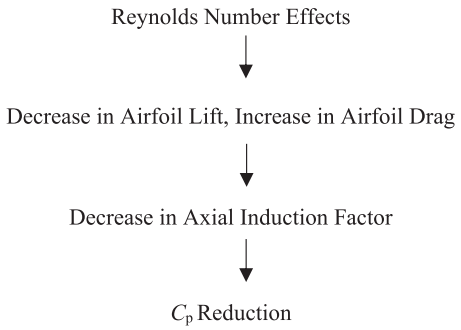


**FIG. 10.** Influence of the Reynolds number on sub-scale turbine aerodynamics for region 2 operations (where $C_p = C_{p,max}$).

### B. Operational results

As previously stated through controller scaling and Eqs. (5) and (12), it is important to match the average tip-speed ratio as well as the average non-dimensional rotational rate despite the aerodynamic alterations stated in Sec. IV A. Matching the tip-speed ratio helps to approximately keep the flow angles over the rotor consistent. An exact match in flow angles over the blade can occur so long as the pitch and axial induction factors remain constant between full- and sub-scales. Matching the non-dimensional rotational rate ensures that the resonant conditions which occur at the full-scale also occur at the sub-scale. The matching tip-speed ratio can be seen in Fig. 8(a) and the matching non-dimensional rotational rate over a range of wind speeds is seen in Fig. 11. As expected, both the tip-speed ratio and non-dimensional rotational rate match over the entire range of wind speeds.

The resulting pitch over a range of wind speeds is depicted in Fig. 12(a). The values match well for the below-rated conditions and are within 10% for above rated conditions due to the system pitching to obtain more power makeup for the higher drag and lower lift due to Reynolds number differences.

To determine how well the scaling performs, the mean and fluctuating values of the normalized flapwise tip deflections are given in Eqs. (23) and (24). Such deflections stem directly from the flapwise bending moments, the blade mass and stiffness distributions, and the pitch controller. In addition, these deflections directly indicate the degree of scaling for aeroelastic behaviors

$$\overline{\delta_{tip}} = \frac{\delta_{tip}}{S}, \tag{23}$$

$$\overline{\delta_{tip,rms}} = \frac{\delta_{tip,rms}}{S}. \tag{24}$$

While there are significant aerodynamic changes in a sub-scale rotor, a SAGE scaled rotor aims to ensure that the aeroelastic interactions remain proper. As such, Fig. 13 presents the tip deflections for

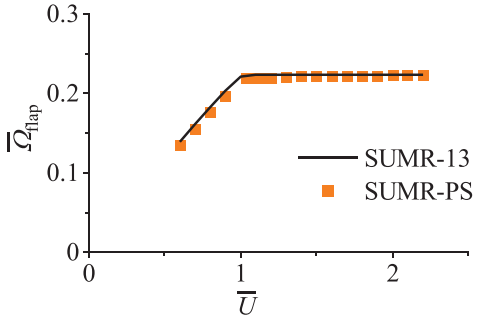


**FIG. 11.** The steady non-dimensional rotational rate ($\bar{\Omega}_{flap}$) over the range of operating steady wind speeds.

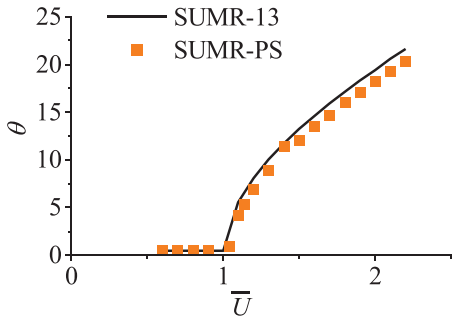


**FIG. 12.** The blade pitch ($\theta$) over a range of operational steady wind speeds.

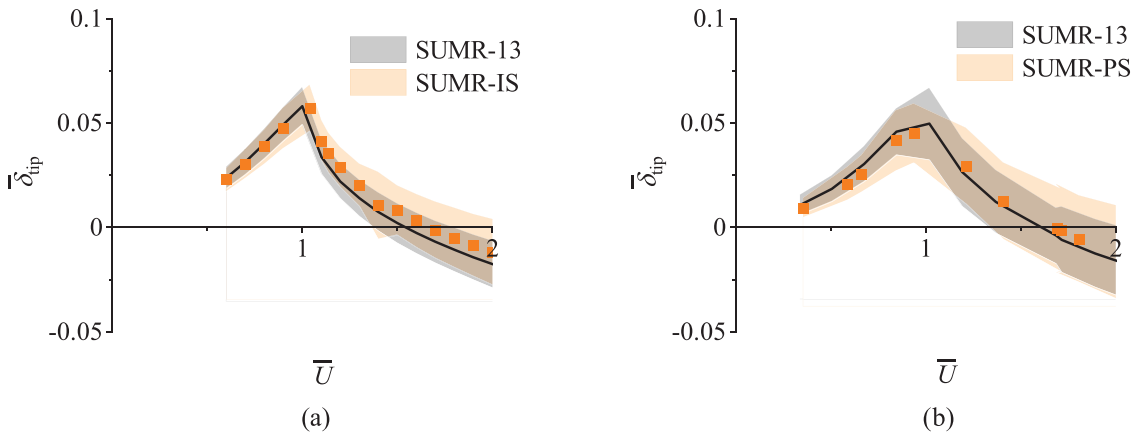


**FIG. 13.** 11 simulations run under (a) steady conditions and (b) turbulent conditions showing the non-dimensional tip deflections ($\overline{\delta}_{tip}$) through the entire range of wind speeds with solid lines representing the average and shaded regions representing one standard deviation above and below this mean.

both the steady and turbulent conditions. Presented are the mean tip deflections as well as the root mean square of tip deflections about the mean. Each case presents below ideal deflections under below-rated conditions and above ideal conditions under above-rated conditions. The turbulent inflow conditions consist of ten evenly spaced average wind speeds ranging from $\overline{U} = 0.35$ to $\overline{U} = 2.1$, where each simulation consists of the useable non-dimensional time, $\overline{t} = 389$, where simulations were given a sufficient amount of time to regulate their operation prior to the usable time. The differences in tip deflection can be attributed to Reynolds effects as well as controller structure differences between below-rated and above-rated conditions. While each mean is slightly different, there is significant overlap of the RMS about the mean and the resultant tip deflections are reasonably accurate despite the significant changes in the Reynolds number.

These results indicate that the inability to match the Reynolds number (and the associated reduction in induction factors at the sub-scale) does not significantly limit the ability to match the aeroelastic deflections for a scaling of 20% on a 13-MW highly flexible downwind turbine when employing the SAGE method. While the objective in this study was to investigate the tip deflections for aeroelasticity, there is also interest in understanding the unsteady blade loads in terms of structural design (to consider on fracture and fatigue). For this, the above methodology could be used to investigate how well the mean and standard deviations of the flapwise loads scale between the two rotors and how the spectra of these loads relative to the blade flapwise natural frequencies. Furthermore, the scaling could be extended to consider edgewise and twist-wise loading on the rotors, as these are also important structural design aspects.

The previous scaling is a strong endorsement for employing sub-scale systems to experimentally study the aeroelastic performance of extreme-scale wind turbine rotor concepts with appropriate servo-gravo-aeroelastic scaling. This is particularly true as the cost of building and testing a research turbine tends to scale with the generated power as well as the rotor mass and a 20% scale turbine has a power rating reduction of more than three orders of magnitude and a mass reduction of 150-fold. The cost savings for a sub-scale turbine may therefore be at least 150-fold. To verify the performance shown in Fig. 13, it is recommended that this approach be assessed by comparing SAGE-based field tests of a full-scale and sub-scale turbine, especially for a lightweight rotor with high flexibility (as is the current trend for extreme-scale rotors), where the load paths tend to significantly deviate from the centrifugally dominated radial direction. It should be noted that fabrication of an aeroelastically scaled rotor has several practical constraints with respect to structural design, material properties, and experimental construction. These aspects have been investigated for a 20% sub-scale manufactured rotor blade.[5] This could be accomplished by employing one of the recent production-level extreme-scale turbines for the full-scale system.[33,34]

Further computational work can be conducted to further examine the effects of Reynolds number by retaining the exact control set points (pitch, non-dimensional RPM, etc.) in reference to a non-dimensional free-stream wind speed. Retaining the control set points will help differentiate between the differences due to aerodynamics and subsequent controls. Additionally, it is suggested to adjust the controller in order to preserve the operational tip deflections of the sub-scale rotor as compared to the full-scale rotor to retain a SAGE scaled rotor.

## V. CONCLUSIONS AND RECOMMENDATIONS

The current study presents an ideal 20% model of a 13.2-MW turbine (SUMR-13) using a servo-aero-gravo-elastic scaling method in order to retain the controller, aerodynamic, and gravitational interactions. The SAGE method aims to match operational conditions by matching the non-dimensional mean wind speeds and their standard deviations. Additionally, the controller is scaled such that the control structure (gain-scheduled, proportional–integral pitch control and variable speed torque control) and the non-dimensional time constant of the pitch control remain constant. Additionally, structural components (blade, tower, hub, etc.) are appropriately scaled such that the non-dimensional structural properties are matched by defining base unit scaling and applying such scaling to the units of a property. Overall, the goal of SAGE scaling is to match the tip-speed ratio, the rotor speed normalized by the flapping frequency, and the average tip deflections during operation normalized by the blade length. The result is the first definition and development of Froude scaling for the rotor moments for an extreme-scale turbine and the first to be

combine Froude scaling for a rotor with aeroelastic scaling or with control-based scaling. The present high-fidelity simulations also represent the first investigation of a Froude-scaled aeroelastic rotor under operational turbulent field conditions.

If one seeks to test a sub-scale and full-scale rotor under field conditions, there are some inherent differences that cannot be accommodate with the present scaling approach. First, there is a difference in the Reynolds and Mach numbers affecting the aerodynamics, which subsequently changes the axial induction factor. These changes due to Reynolds number were concluded to be the primary cause of these differences through testing a sub-scale model which employs the same aerodynamics coefficients as the full-scale model, thus removing any effects of Reynolds numbers. Second, the gain scaling of pitch control though non-dimensionally reasonable (magnitude and bandwidth difference of about 5%) does not consider second-order aeroelastic effects. Furthermore, scaling the mean and turbulence levels for the flow with given atmospheric boundary layer properties can lead to some differences in local shear and turbulent scale coherence arising from different hub-heights. Despite such limitations, the sub-scale turbine under steady and turbulent operational conditions was able to reasonably portray non-dimensional flapwise tip deflections and dynamics observed for the full-scale turbine, which is the primary goal of the SAGE scaling method. These simulations show that the effects of Mach and Reynolds numbers, aeroelastic influence on gains scaling, and coherence characteristics of the atmospheric boundary layer are relatively weak for a 20% sub-scale turbine relative to an advanced-design extreme-scale wind turbine using the present scaling methodology. This indicates the high potential value of employing sub-scale systems to experimentally study the aeroelastic performance of extreme-scale wind turbine rotor concepts with appropriate servo-gravo-aeroelastic scaling. However, experimental field testing is recommended to confirm the quantitative efficacy of this scaling methodology. In addition, further work can be conducted computationally to further examine the effects of Reynolds number by investigating adjustment to control set points and pitch controller gains to further improve the consistency between the non-dimensional operational tip deflections and dynamics of the sub-scale and full-scale rotor to reproduce all the key servo-aero-gravo-elastic characteristics of the turbine response and performance.

## ACKNOWLEDGMENTS

The authors would like to acknowledge Daniel (Todd) Griffith, Juliet Simpson, Sepideh Kianbakht, and Dana Martin for comments and suggestions throughout the research study. This work has been supported by ARPA-E under Award No. DE-AR0000667. Any opinions, findings, and conclusions or recommendations expressed in this material are those of the authors and do not necessarily reflect the views of ARPA-E.

## DATA AVAILABILITY

The data that support the findings of this study are available from the corresponding author upon reasonable request.

## REFERENCES

[1]R. Wiser *et al.*, *Wind Technologies Market Report* (U.S. Department of Energy, 2018).
[2]G. Bir and J. M. Jonkman, "Aeroelastic instabilities of large offshore and onshore wind Turbinesa," J. Phys. **75**, 012069 (2007).
[3]C. Noyes, C. Qin, and E. Loth, "Pre-aligned downwind rotor for a 13.2 MW wind turbine," Renewable Energy **116**, 749–754 (2018).
[4]G. K. Ananda, S. Bansal, and M. S. Selig, "Aerodynamic design of the 13.2 MW SUMR-13i wind turbine rotor," in AIAA SciTech Forum (2018).
[5]E. Loth *et al.*, "Downwind pre-aligned rotors for extreme-scale wind turbines," Wind Energy **20**, 1241–1259 (2017).
[6]M. Chetan, D. Todd Griffith, and S. Yao, "Flutter predictions in the design of extreme-scale segmented ultralight morphing rotor blades" in AIAA Sci TechForum.
[7]D. T. Griffith and T. D. Ashwill, "The Sandia 100-meter all-glass baseline wind turbine blade: SNL100-00," Baseline Report No. SAND2011-3779 (2011).
[8]D. T. Griffith, "The SNL100-01 blade: Carbon design studies for the Sandia 100-meter blade," Report No. SAND2013-1178 (2013).
[9]D. T. Griffith, "The SNL100-02 blade: Advanced core material design studies for the Sandia 100-meter blade," Report No. SAND2013-10162 (2013).
[10]D. T. Griffith and P. W. Richards, "The SNL100-03 blade: Design studies with flatback airfoils for the Sandia 100-meter blade," Report No. SAND2014-18129 (2014).
[11]E. Loth, M. S. Selig, and P. Moriarty, "Morphing segmented wind turbine concept," in AIAA Applied Aerodynamics Conference (2010), pp. 1–6.
[12]E. Loth, A. Steele, B. Ichter, M. S. Selig, and P. Moriarty, "Segmented ultralight pre-aligned rotor for extreme-scale wind turbines," in AIAA Aerospace Sciences Meeting (2012).
[13]C. Noyes, C. Qin, and E. Loth, "Ultralight, morphing rotor for extreme-scale wind turbines," in AIAA SciTech Forum (2017).
[14]M. Kaminski, E. Loth, D. T. Griffith, and C. C. Qin, "Ground testing of a 1% gravo-aeroelastically scaled additively-manufactured wind turbine blade with bio-inspired structural design," J. Renewable Energy **148**, 639–650 (2020).
[15]C. L. Bottasso, F. Campagnolo, and V. Petrović, "Wind tunnel testing of scaled wind turbine models: Beyond aerodynamics," J. Wind Eng. Ind. Aerodyn. **127**, 11–28 (2014).
[16]I. Bayati, M. Belloli, L. Bernini, and A. Zasso, "Aerodynamic design methodology for wind tunnel tests of wind turbine rotors," J. Wind Eng. Ind. Aerodyn. **167**, 217–227 (2017).
[17]D. P. Martin, K. E. Johnson, D. S. Zalkind, and L. Y. Pao, "LPV-based torque control for an extreme-scale morphing wind turbine rotor," in Proceedings of the American Control Conference (2017), pp. 1383–1388.
[18]S. McTavish, D. Feszty, and F. Nitzsche, "Evaluating Reynolds number effects in small-scale wind turbine experiments," J. Wind Eng. Ind. Aerodyn. **120**, 81 (2013).
[19]M. Make and G. Vaz, "Analyzing scaling effects on offshore wind turbines using CFD," Renewable Energy **83**, 1326–1340 (2015).
[20]S. Yao *et al.*, "Structural design of a 1/5th scale gravo-aeroelastically scaled wind turbine demonstrator blade for field testing," in AIAA SciTech Forum (2019), pp. 1–9.
[21]C. J. Bay *et al.*, "Design and testing of a scaled demonstrator turbine at the National Wind Technology Center," in AIAA SciTech Forum (2019).
[22]M. Kaminski *et al.*, "Gravo-aeroelastic scaling of a 13-MW downwind rotor for 20% scale blades" Wind Energy **2020**, 1–7.
[23]J. M. Jonkman, S. Butterfield, W. Musial, and G. Scott, "Definition of a 5-MW reference wind turbine for offshore system development," Technical Report No. NREL/TP-500-38060 (2009).
[24]D. S. Zalkind, E. Dall'Anese, and L. Y. Pao, "Automatic controller tuning using a zeroth-order optimization algorithm," Wind Energy Sci. Discuss. (published online, 2020).
[25]M. Hansen, J. Sørensen, S. Voutsinas, N. Sørensen, and H. Madsen, "State of the art in wind turbine aerodynamics and aeroelasticity," Prog. Aerosp. Sci. **42**, 285–330 (2006).
[26]E. A. Bossanyi, "Wind turbine control for load reduction," Wind Energy **6**, 229–244 (2003).
[27]L. Y. Pao and K. E. Johnson, "Control of wind turbines: Approaches, challenges, and recent developments," IEEE Control Syst. Mag. **31**, 44–62 (2011).
[28]F. Dunne, J. Aho, and L. Y. Pao, "Analysis of gain-scheduling implementation for the NREL 5-MW turbine blade pitch controller," in 2016 Proceedings of the American Control Conference, July (2016), pp. 3188–3193.

[29]J. M. Jonkman and M. L. Buhl, Jr., *FAST User's Guide* (NREL, 2005).
[30]M. Drela, "XFOIL: An analysis and design system for low Reynolds number airfoils," in *Low Reynolds Number Aerodynamics, Lecture Notes Engineering* (Springer, 1989), Vol. 54.
[31]J. M. Jonkman and L. Kilcher, *TurbSim User's Guide: Version 1.06.00* (NREL, 2012).
[32]N. K. Kohli and L. K. Patel, "Study of performance of wind turbine," Int. J. Latest Technol. Eng. **1**, 2ICAE-2012 (2012).
[33]See https://www.ge.com/renewableenergy/wind-energy/offshore-wind/haliade-x-offshore-turbine for "GE. Haliade-X 12 MW Offshore Wind Turbine Platform."
[34]V. Diaz, see https://www.siemensgamesa.com/en-int/newsroom/2020/05/200519-siemens-gamesa-turbine-14-222-dd# for "Powered by Change: Siemens Gamesa Launches 14 MW Offshore Direct Drive Turbine with 222-Meter Rotor, With an Unprecedented 14-MW, World Currently Undergoing Enormous Upheaval, 2020."